Journal of Hydrology 391 (2010) 34–46

Contents lists available at ScienceDirect

Journal of Hydrology

journal homepage: www.elsevier.com/locate/jhydrol

Numerical simulation of meandering evolution

Jennifer G. Duan [a,*], Pierre Y. Julien [b]

[a] Department of Civil Engineering and Engineering Mechanics, 1209 E. 2nd Street, Tucson, AZ 85721, USA
[b] Department of Civil and Environmental Engineering, Colorado State University, Fort Collins, CO, USA

ARTICLE INFO

Article history:
Received 16 July 2009
Received in revised form 7 June 2010
Accepted 4 July 2010

This manuscript was handled by Konstantine P. Georgakakos, Editor-in-Chief, with the assistance of Kieran M. O'Connor, Associate Editor

Keywords:
Meandering channel
Sediment transport
River mechanics
Bank erosion
Numerical modeling

SUMMARY

A two-dimensional depth-averaged hydrodynamic model is developed to simulate the evolution of meandering channels from the complex interaction between downstream and secondary flows, bed load and suspended sediment transport, and bank erosion. The depth-averaged model calculates both bed load and suspended load assuming equilibrium sediment transport and simulates bank erosion with a combination of two interactive processes: basal erosion and bank failure. The mass conservation equation is solved to account for both vertical bed-elevation changes as well as lateral migration changes when sediment is removed through basal erosion and bank failure. The numerical model uses deformable elements and a movable grid to simulate the gradual evolution of a near-straight deformable channel into a highly sinuous meandering channel. The model correctly replicates the different phases of the evolution of free meandering channels in experimental laboratory settings including: (1) downstream and upstream migration; (2) lateral extension; and (3) rotation of meander bends.

© 2010 Elsevier B.V. All rights reserved.

1. Introduction

The evolution of meandering channels involves the complex interaction of fluid dynamics, sediment transport, and bank erosion. Flow converges to the concave banks and diverges near convex banks due to the secondary flows in meandering channels. Flow momentum redistribution causes bed degradation near concave banks and deposition near convex banks. Bed degradation steepens concave banks while deposition stabilizes convex banks. This causes concave banks to retreat as bank erosion occurs, while convex banks advance with the build up of point bars. Consequently, the planform of meandering channel evolves as meandering loops migrate to downstream. Due to the limitation of detailed experimental and field data of flow and sediment transport, this study aims to examine flow and sediment transport during the meandering processes using a two-dimensional numerical model.

With the rapid development of mathematical models and advances in computer technology, one-, two- and three-dimensional, computational fluid dynamic models have become increasingly popular to simulate the morpho-dynamic processes of natural rivers (Darby et al., 2002); meandering streams (Mosselman, 1998; Duan et al., 2001; Olsen, 2003); and braiding channels (Nicholas and Smith, 1999). Meandering models (Ikeda et al., 1981; Johannesson and Parker, 1989; Sun et al., 1996; Zolezzi and Seminara, 2001; Camporeale et al., 2005) employed the quasi-two dimensional analytical solutions of Navier–Stokes equation and assumed the bank erosion rate proportional to near bank excessive velocity. These models have limitations due to linear solutions of flow field and neglecting sediment transport field near banks. On the other hand, flow patterns and velocity profiles have been examined with depth-integrated models by Zarrati et al. (2005), and also in sine-generated meandering streams by da Silva et al. (2006). A full three-dimensional computational fluid dynamic model has been successfully applied to simulate the formation of meandering streams (Olsen, 2003; Wilson et al., 2003). More recent contributions focused on the diffusion and dispersion characteristics in meander bends using transient tracer tests (Baek et al., 2006; Marion and Zaramella, 2006; Seo et al., 2008).

Several models can simulate bank erosion and lateral migration of alluvial channels. Among them Mosselman (1998) simulated the morpho-dynamic processes of the Ohre River, a meandering gravel-bed in the former state of Czechoslovakia. Darby et al. (2002) replaced the bank erosion subroutine within the two-dimensional, depth-averaged numerical model RIPA with the Osman and Thorne (1988) bank erosion algorithm to simulate the bank erosion processes at the Goodwin Creek, Mississippi. Duan et al. (2001) and Duan and Julien (2005) developed a two-dimensional, depth-averaged hydrodynamic and sediment transport model and

* Corresponding author.
E-mail addresses: gduan@email.arizona.edu (J.G. Duan), Pierre@engr.colostate.edu (P.Y. Julien).

0022-1694/$ - see front matter © 2010 Elsevier B.V. All rights reserved.
doi:10.1016/j.jhydrol.2010.07.005

Nomenclature

$\frac{\partial z_b}{\partial n}$	transverse slope
a	reference bed level
$B = 8.47 \pm 0.9$	integration constant
$C_m = 8.0$	coefficient
C and C_a	suspended sediment concentrations and value at $z = a$, respectively
C_*	depth-averaged equilibrium concentrations of suspended sediment
C'_L	lift coefficient
D_{uu}, D_{uv}, and D_{vv}	dispersion terms from the discrepancy between the depth-averaged velocity and the actual velocity in Cartesian coordinates
D^c_{uu}, D^c_{uv}, and D^c_{vv}	dispersion terms in curvilinear coordinates
$D_* = d_{50} \cdot \left[\frac{(s-1)g}{\nu^2}\right]^{\frac{1}{3}}$	dimensionless particle diameter
dr	width of the control volume nearest to the edge of the bank
d_{50}	median particle diameter
E	erosion coefficient with a unit of $(\mathrm{m}^3/\mathrm{kg})^{1/2}$ in SI system
h	flow depth
h_b	near-bank flow depth
g	gravitational acceleration
K_1 and K_2	coefficients accounting for the effects of longitudinal and transverse slopes, respectively
k_s	roughness height and equals the median particle diameter
N_*	a coefficient equal to 7.0 derived by Engelund (1974)
n	Manning roughness coefficient
p	porosity of bed and bank material
q_b	bed-load sediment transport per unit width
$R^*_e = \frac{u_* d_{50}}{\nu}$	particle Reynolds number
R_n	Rouse number
q_{bx} and q_{by}	bed-load transport components in the x and y directions, respectively
q_{sx} and q_{sy}	suspended load components in the x and y directions, respectively
q^b_{br}	net volume of sediment from bank erosion
q_l and q_r	sediment transport rates in the longitudinal and transverse directions, respectively
$q_{br} = q^b_{br} + q^f_{br}$	transverse component of the sediment transport rate at the near-bank region as a result of bank erosion
q_{sl} and q_{sr}	suspended sediment transport rates in the longitudinal and transverse directions, respectively
q^f_{br}	sediment material eroded per unit width from bank failure
r	channel radius of curvature
$s = \frac{\rho_s}{\rho}$	specific gravity
$T = \frac{\tau_* - \tau_{*c}}{\tau_{*c}}$	dimensionless transport parameter
t	time
U	depth-averaged total velocity
$\overline{u}$ and $\overline{v}$	depth-averaged velocity components in the x and y directions, respectively
u_*	shear velocity
u_l and $\overline{u_l}$	local and depth-averaged streamwise velocities, respectively
u_{bn} and u_{bs}	near-bed transverse and longitudinal velocities, respectively
v_r, $\overline{v}_r$, and v_s	transverse velocity, depth-averaged transverse velocity, and transverse velocity at the water surface, respectively
z_0	zero velocity level
z and z_0	actual and reference elevations above bed, respectively
z_b	bed elevation
Δh_{bank}	bank height above the water surface
$\alpha = 0.85$	friction coefficient
α_x and α_y	fractional components of bed-load transport in the x and y directions, respectively
β	deviation angle of near bed velocity
β'	ratio of the diffusion of sediment to fluid turbulent diffusion
β_1	longitudinal bed-slope angle
β_2	transverse bed-slope angle
ε	bank erosion rate
ζ	surface elevation
θ	angle between the centerline and positive x axis
$\kappa = 0.41$	von-Karman constant
$\lambda_s = 0.59$	friction coefficient
$\mu = \tan\phi$	friction coefficient
μ'	a factor to address bedform effects
ν_t	eddy viscosity
$\overline{\xi}$	depth-averaged bank erosion rate due to hydraulic force
ρ_s and ρ	mass densities of sediment and water, respectively
$\overline{\delta}$	averaged bank slope angle
τ_{bx} and τ_{by}	friction shear stress terms at the bottom in the x and y directions, respectively
τ_{xy}, τ_{xx}, τ_{yx}, and τ_{yy}	Reynolds shear stress terms
$\tau_* = \frac{\rho u_*^2}{(\rho_s - \rho) g d_{50}}$	Shields parameter
$\tau_{*c} = \frac{\tau_c}{(\rho_s - \rho) g d_{50}}$	critical value of τ_* on sloping bed
$\tau_{*c,0}$	critical Shields parameter on a horizontal bed
ϕ	angle of repose
ω	fall velocity

successfully simulated the initiation, evolution, and widening of meandering channels.

However, there are several remaining questions regarding the fundamental physical processes that govern meandering evolution. For instance, it is not clear that numerical models can properly simulate the formation of meandering channels. The complete simulation of the various modes of deformation of meandering channels such as downstream and upstream migration, lateral extension and rotation of meander bends has not been reported in literature. Furthermore, the mechanism that governs the evolutions of meandering rivers (e.g. flow, sediment, bank erosion) has not been fully understood. This research has been undertaken to demonstrate that a simple two-dimensional numerical model can be an effective tool to study the mechanism of meandering evolution. The earlier developments of the two-dimensional, depth-averaged hydrodynamic and sediment transport model (Duan and Nanda, 2006; Duan and Julien, 2005; Duan, 2004) are extended to simulate the evolution patterns of meandering channels. The main hypothesis of this research is that meandering planform geometry and variations in bed bathymetry caused the redistribution of flow momentum and consequently the migration of meandering channels.

This article specifically focuses on the numerical simulation of meandering channel planform changes at different stages of their evolution. The objective is to demonstrate that 2D numerical models of deformable meandering channels can properly simulate the various types of deformation including downstream and upstream migration, lateral extension, and rotation of meander bends. A brief review of the flow and sediment transport algorithms is followed by a description of the bank erosion and channel deformation mechanics. The results of the model link the processes of bed topography and flow momentum with the processes of deformation of

meandering channels including upstream and downstream migration, lateral extension and rotation of deformable channels.

2. Flow simulation algorithm

The governing equations for flow simulation are the depth-averaged Reynolds approximation of momentum equations (Eqs. (1) and (2)) and continuity equation (Eq. (3)).

$$\frac{\partial(h\overline{u})}{\partial t}+\frac{\partial}{\partial x}(h\overline{u}^2)+\frac{\partial D_{uu}}{\partial x}+\frac{\partial}{\partial y}(h\overline{u}\overline{v})+\frac{\partial D_{uv}}{\partial y} = -gh\frac{\partial\zeta}{\partial x}+\frac{\partial}{\partial x}(h\tau_{xx})+\frac{\partial}{\partial y}(h\tau_{xy})-\tau_{bx} \quad (1)$$

$$\frac{\partial(h\overline{v})}{\partial t}+\frac{\partial}{\partial x}(h\overline{u}\overline{v})+\frac{\partial D_{uv}}{\partial x}+\frac{\partial}{\partial y}(h\overline{v}^2)+\frac{\partial D_{vv}}{\partial y} = -gh\frac{\partial\zeta}{\partial y}+\frac{\partial}{\partial x}(h\tau_{yx})+\frac{\partial}{\partial y}(h\tau_{yy})-\tau_{by} \quad (2)$$

$$\frac{\partial h}{\partial t}+\frac{\partial}{\partial x}(h\overline{u})+\frac{\partial}{\partial y}(h\overline{v})=0 \quad (3)$$

where $\overline{u}$ and $\overline{v}$ are depth-averaged velocity components in the x and y directions, respectively; t is time; ζ is surface elevation; h is flow depth; g is acceleration of gravity; τ_{bx} and τ_{by} are friction shear stress terms at the bottom in the x and y directions, respectively, written as $\tau_{bx}=n^2g/h^{\frac{1}{3}}\overline{u}U$ and $\tau_{by}=n^2g/h^{\frac{1}{3}}\overline{v}U$, in which U is depth-averaged total velocity and n is Manning's roughness coefficient; τ_{xy}, τ_{xx}, τ_{yx}, and τ_{yy} are depth-averaged Reynolds stress terms, which are expressed as $\tau_{xx}=2\nu_t\partial\overline{u}/\partial x$, $\tau_{yy}=2\nu_t\partial\overline{v}/\partial y$, $\tau_{xy}=\tau_{yx}=\nu_t(\partial\overline{u}/\partial y+\partial\overline{v}/\partial x)$, in which ν_t is eddy viscosity; and D_{uu}, D_{uv}, and D_{vv} are dispersion terms resulting from the discrepancy between the depth-averaged velocity and the actual velocity in the Cartesian coordinate, which are calculated by using the dispersion terms at the streamwise and transverse directions as follows:

$$D^c_{uu}=\int_{z_0}^{z_0+h}(u_l-\overline{u_l})^2dz;\ D^c_{uv}=\int_{z_0}^{z_0+h}(u_l-\overline{u_l})(v_r-\overline{v_r})dz;\ D^c_{vv}=\int_{z_0}^{z_0+h}(v_r-\overline{v_r})^2dz \quad (4)$$

where D^c_{uu}, D^c_{uv}, and D^c_{vv} denote dispersion terms in curvilinear coordinates, and z_0 is the zero velocity level.

The depth-averaged parabolic eddy viscosity model is adopted, where the depth-averaged eddy viscosity is obtained as follows:

$$\nu_t=\frac{1}{6}\kappa u_* h \quad (5)$$

where u_* is shear velocity and κ is the von-Karman constant. Eventually, more sophisticated turbulent model components could be developed to improve the accuracy of the two-dimensional modeling results.

To include the effect of secondary flow, four dispersion terms were added to the momentum equations. The mathematical expressions of these terms are derived after assuming that the streamwise velocity satisfies the logarithmic law for uniform flows over well-packed gravel-beds (Kironoto and Graf, 1994). The streamwise velocity profile can then be written as follows:

$$\frac{u_l}{\overline{u_l}}=\frac{\frac{1}{\kappa}ln\left(\frac{z+z_0}{k_s}\right)+B}{\frac{1}{\kappa}\left(ln\frac{h}{k_s}-1+\frac{k_s}{h}\right)+B\left(1-\frac{k_s}{h}\right)} \quad (6)$$

where u_l and $\overline{u_l}$ are respectively the streamwise and depth-averaged streamwise velocities; z and z_0 are the actual and reference elevations above bed; h is flow depth; $\kappa=0.41$ is the von-Karman constant; k_s is the roughness height and equals the mean-sized sediment particle; and B is a constant of integration and is typically equal to 8.47 ± 0.9 (Kironoto and Graf, 1994). The transverse velocity profile of the secondary flow is assumed to be linear. The profile of the transverse velocity proposed by Odgaard (1989) was adopted in this model.

$$v_r=\overline{v_r}+2v_s\left(\frac{z}{h}-\frac{1}{2}\right) \quad (7)$$

where v_r, $\overline{v_r}$, and v_s are the transverse velocity, depth-averaged transverse velocity, and transverse velocity at the water surface, respectively. Engelund (1974) derived the tangent of the deviation angle of the bottom shear stress and gave the following expression:

$$\left(\frac{\tau_r}{\tau_l}\right)_b\approx\left(\frac{v_r}{u_l}\right)_b=7.0\frac{h}{r} \quad (8)$$

where r is the radius of channel curvature. This formulation is similar to the classical formulation of Rozovskii, also discussed in Julien (2002). According to Eq. (7), the magnitude of the deviation of secondary flow velocities from the mean transverse velocity at the surface and the bottom are equal. Therefore, Eq. (8) (Engelund, 1974) was used as the transverse velocity at the surface. The dispersion terms, D^c_{uu}, D^c_{uv}, and D^c_{vv}, were calculated by substituting Eqs. (6) and (7) into Eq. (4), and then decomposed into the x and y direction in the Cartesian coordinates in Eqs. (1) and (2) to solve for flow velocity. A more detailed description of the hydrodynamic model was included in Duan (2004).

3. Sediment transport algorithm

3.1. Bed-load transport

To predict bed-load transport in a curved channel, at least three forces should be considered. These forces include: (1) the bed-shear stress in the longitudinal direction; (2) the lateral bed-shear stress due to curvature-induced secondary flow in the transverse direction; and (3) the lateral component of the gravitational force on the sloping channel bed, or bank. The influence of gravity on bed-load transport is reflected in terms of its effect on incipient motion of sediment and the direction of bed-load transport.

Numerous equations are available to predict the bed-load transport rate. In the present study, we selected the Meyer-Peter and Muller's bed-load transport formula, which is valid for uniform sediment having a mean particle size ranging from 0.23 to 28.6 mm. The bed-load transport rate was computed with this formula as follows:

$$q_b=C_m[(s-1)g]^{0.5}d_{50}^{1.5}(\mu'\tau_*-\tau_{*c})^{1.5} \quad (9)$$

where q_b is the total bed-load transport rate per unit width; $\tau_*=\rho u_*^2/(\rho_s-\rho)gd_{50}$ is the effective particle mobility parameter; $\tau_{*c}=\tau_c/(\rho_s-\rho)gd_{50}$ is the critical value of τ_* for incipient motion depending on the particle Reynolds number ($R_e^*=u_*d_{50}/\nu$), and $\tau_{*c}=0.047$ when $R_e^*>100$; the constant coefficient $C_m=8.0$; d_{50} is the mean particle diameter; and $s=\rho_s/\rho$, where ρ_s and ρ are densities of sand and water, respectively. The bed surface is assumed to be free of bed forms and the factor for bed form resistance, $\mu'=1$, is used in this model.

Bed-load transport is known to deviate from the downstream flow direction because of the influence of secondary flows, and the lateral shear stress and gravitational effects on the transverse bed slope. The deviation angle is defined as the angle between the centerline of the channel and the direction of shear force at the bed. Engelund (1974), Bridge and Bennett (1992), and Darby and Delbono (2002) derived relations to estimate the deviation

angle based on the analytical solutions of flow field in sinuous channels. Bridge and Bennett (1992) and Darby and Delbono (2002) stressed in their relations that flow in the bend with a varying curvature is non-uniform, so steady and non-uniform flow momentum equations are necessary when solving the flow field. As a result, the tangent of the deviation angle (Darby and Delbono, 2002) is not only a function of the mean longitudinal and transverse velocity components, local radii of curvature and friction, but also varies spatially in sine-generated bends. This study adopted the deviation angle, β, written as follows:

$$\tan\beta = \frac{u_{br}}{u_{bl}} - \frac{1+\alpha\mu}{\lambda_s\mu}\sqrt{\frac{\tau_{*c}}{\tau_*}}\frac{\partial z_b}{\partial n} = -N_*\frac{h}{r} - \frac{1+\alpha\mu}{\lambda_s\mu}\sqrt{\frac{\tau_{*c}}{\tau_*}}\frac{\partial z_b}{\partial n} \tag{10}$$

where u_{br} and u_{bl} are the near-bed transverse and longitudinal velocities, respectively; $\alpha = 0.85$, $\mu = \tan\phi$, and $\lambda_s = 0.59$ are friction coefficients, in which ϕ is the angle of repose; r is the radius of the curvature; N_* is a coefficient that equals 7.0 derived by Engelund (1974); and $\partial z_b/\partial n$ denotes the transverse slope. The first term on the right of Eq. (10) accounts for the effect of secondary flow velocity at the bottom, and the second term quantifies the gravitational effects of the transverse bed slope. Therefore, the direction of bed-load transport in Cartesian coordinates denoted by x and y can be obtained as follows:

$$\begin{bmatrix} a_x \\ a_y \end{bmatrix} = \begin{bmatrix} \sin\beta & \cos\beta \\ cos\beta & -\sin\beta \end{bmatrix}\begin{bmatrix} \sin\theta \\ cos\theta \end{bmatrix} \tag{11}$$

where θ is the angle between the centerline and positive x axis; β is the deviation angle; and α_x and α_y denote the fractional components of bed-load transport in the x and y directions, respectively.

The critical shear stress of sediment particles on a longitudinally and transversely sloped bed is correlated to the critical shear stress of the same sized particle on the flat bed as follows (van Rijn, 1989):

$$\tau_{*c} = K_1K_2\tau_{*c,0} \tag{12}$$

where τ_{*c} and $\tau_{*c,0}$ are the critical shear stress on sloping and horizontal beds, respectively; K_1 and K_2 are coefficients accounting for the effects of longitudinal and transverse slopes, respectively. The coefficient K_1 is defined as

$$K_1 = \sin(\phi-\beta_1)/\sin\phi \text{ (for a downsloping bed)} \tag{13}$$

$$K_1 = \sin(\phi+\beta_1)/\sin\phi \text{ (for an upsloping bed)} \tag{14}$$

where ϕ is the angle of repose; and β_1 is the longitudinal bed-slope angle. Whereas $K_2 = [\cos\beta_2][1-(\tan^2\beta_2/\tan^2\phi)]^{0.5}$, and β_2 is the transverse bed-slope angle. More details on the expressions of K_1 and K_2 can be found in Julien and Anthony (2002) and Duan and Julien (2005).

3.2. Suspended sediment transport

To calculate the rate of suspended sediment transport, a suspended sediment concentration profile must be assumed. In this model, the classic Rouse profile (van Rijn, 1989) is assumed to be valid at $z = a$ from the channel bed to the water surface. The Rouse profile is written as follows:

$$\frac{C}{C_a} = \left(\frac{h-z}{z}\frac{a}{h-a}\right)^{R_n} \tag{15}$$

where a is the reference bed level; z is the distance from the bottom; R_n is the Rouse number; and C and C_a are concentrations of suspended sediment with their values at $z = a$, respectively. The expression of the Rouse number is given as follows:

$$R_n = \frac{\omega}{\kappa\beta' u_*} \tag{16}$$

where R_n is the Rouse number; ω is the falling velocity; $\kappa = 0.4$ is the von-Karman constant; u_* is the shear velocity; and β' describes (van Rijn, 1989) the difference in the diffusion of a sediment particle from the diffusion of a fluid "particle" (Duan and Julien, 2005; Duan and Nanda, 2006). The suspended sediment transport rate is the product of the velocity profile and suspended sediment concentration profile.

The van Rijn formula (1989) was adopted here for computing the reference concentration as follows:

$$C_a = 0.015\frac{d_{50}}{a}\frac{T^{1.5}}{D_*^{0.3}} \tag{17}$$

where $D_* = d_{50'}\left[(s-1)g/\nu^2\right]^{\frac{1}{3}}$ is the dimensionless particle diameter and $T = \tau_* - \tau_{*c}/\tau_{*c}$ where τ_* is the dimensionless grain shear-stress parameter and τ_{*c} is the critical bed-shear stress according to Eq. (12). By knowing the longitudinal and transverse velocity profiles (Eqs. (6) and (7)) and the concentration of suspended sediment (Eq. (15)), the suspended sediment transport rates in the longitudinal and transverse directions can be obtained as follows:

$$q_{sl} = \int_{z_0}^{z_0+h} u_l C\,dz;\ q_{sr} = \int_{z_0}^{z_0+h} v_r C\,dz; \tag{18}$$

where q_{sl} and q_{sr} are the suspended sediment transport rates in the longitudinal and transverse directions, respectively. Because the Cartesian coordinates are used in this model, the longitudinal and transverse components of the suspended sediment transport rate were transformed into the x and y Cartesian coordinate components according to Eq. (11).

4. Channel deformation algorithm

4.1. Bed-elevation changes

To simulate channel bed degradation or aggradation, the bed-load transport rate is linked with the mass conservation equation. The sediment continuity equation is then used for calculating bed-elevation changes as follows:

$$(1-p)\frac{\partial z_b}{\partial t} + \frac{\partial(q_{bx}+q_{sx})}{\partial x} + \frac{\partial(q_{by}+q_{sy})}{\partial y} = 0 \tag{19}$$

where p is porosity of bed and bank material; z_b is bed elevation; q_{bx} and q_{by} are components of bed-load transport rate in the x and y directions, respectively; and q_{sx} and q_{sy} are components of total suspended loads in the x and y directions, respectively.

4.2. Bank erosion

Bank erosion consists of two interactive physical processes: basal erosion and bank failure (Osman and Thorne, 1988). Basal erosion refers to the fluvial entrainment of bank material removal by the near-bed hydrodynamic forces. Bank failure occurs due to geotechnical instability (e.g., planar failure, rotational failure, sapping, or piping). The present model separates the calculation of bank erosion and the advance and retreat of bank lines. Sediment from basal erosion is calculated by using an analytical approach derived in Duan et al. (2001) and Duan (2005). Mass wasting from bank failure is calculated using the parallel bank-failure model for non-cohesive bank material.

4.3. Basal erosion

The depth-averaged bank erosion rate is the difference between the entrainment and deposition of bank material calculated by Eq. (20) and (21) derived in Duan (2005).

$$\overline{\xi} = E\left(1 - \frac{\tau_{bc}}{\tau_{b0}}\right)^{\frac{3}{2}} \sqrt{\tau_{b0}} \tag{20}$$

$\overline{\xi}$ is the depth-averaged bank erosion rate due to hydraulic force, τ_{bc} and τ_{b0} are the critical shearing stress of bank material and the actual bed-shear stress at the bank toe, respectively; and E is the erosion coefficient with a unit of $(m^3/kg)^{1/2}$ in SI system, which relates to the averaged bank angle, coefficient of lift force, the depth-averaged and equilibrium concentration of suspended sediment, which is calculated as

$$E = \sin\overline{\delta}\sqrt{\frac{C_L'}{3\rho_s}}\left(1 - \frac{C}{C_*}\cos\overline{\delta}\right) \tag{21}$$

where $\overline{\delta}$ is the averaged bank slope angle; C_L' is the lift coefficient obtained as $C_L' = C_L \ln^2(0.35d/k_s)/\kappa^2$, in which $C_L = 0.178$, a constant for turbulent flow, κ is von-Karman constant, and k_s is the roughness height equal to the mean size of sand grain (Chien and Wan, 1991); ρ_s is the density of sediment particles; C and C_* are the depth-averaged and equilibrium concentrations of suspended sediment, respectively; The mass volume contributing to the main channel from basal erosion can be calculated as follows:

$$q_{br}^b = \frac{\overline{\xi}(1-p)h_b}{\sin\overline{\delta}} \tag{22}$$

where q_{br}^b is the net volume of sediment contributed to the main channel from bank erosion and h_b is the flow depth at the near-bank region. To account for porosity p in the bank material, the factor $1-p$ is multiplied. If $\overline{\xi} = 0$, the riverbank is not undergoing erosion, so the near-bank, suspended sediment concentration reaches the value of equilibrium. The term $\sin\overline{\delta}$ converts the distance of bank erosion to the volumetric net bank material from basal erosion.

4.4. Mass failure for non-cohesive bank material

Pizzuto (1990) derived and applied a slumping bank-failure model for non-cohesive bank material, which was later modified by Nagata et al. (2000). Fluvial erosion degrades the channel bed and destabilizes the upper bank until the bank angle exceeds the angle of repose for bank material. The slumping bank-failure model requires the bank-failure surface to be inclined at the angle of repose projected to the floodplain. In the present study, the slumping bank-failure model was combined with the parallel retreat method that assumes the newly formed bank surface after bank failure is always parallel to the old surface (Chen and Duan, 2008). It assumes that mass wasting from bank failure is the product of the rate of basal erosion and height of bank surface above the water surface. Therefore, the amount of bank material from mass failure is calculated as follows:

$$q_{br}^f = \overline{\xi}\Delta h_{bank}(1-p) \tag{23}$$

where q_{br}^f is sediment material eroded per unit channel length from bank failure, and Δh_{bank} is bank height above the water surface.

4.5. Advance and retreat of bank lines

Meandering migration consists of the retreat of concave banks and advances of convex banks. Bank erosion causes bankline retreat. Advance is caused by the sediment deposition near the bank. The deposited sediment can be supplied from eroded bank or bed material transported from the upstream region. A bank retreats as the material is transported away by flow. Predicting bank advance or retreat is based on a balance (or mass conservation) of the sediment in a control volume near the bank, including sediment from bank erosion and failure, sediment stored on the bed due to deposition, and sediment fluxes transported in and out of the control volume. The rate of bank advance or retreat shown in Fig. 1 can be calculated as follows (Duan et al., 2001; Duan and Julien, 2005):

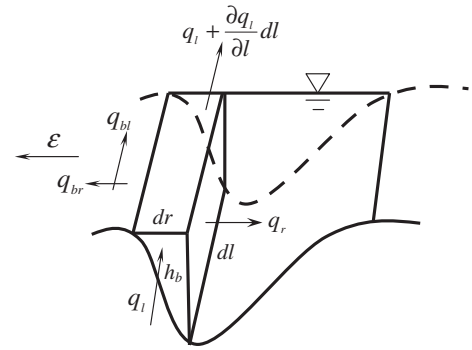

Fig. 1. Near-bank control volume for bank erosion calculation.

$$\varepsilon = -\frac{\left(\frac{\partial q_l}{\partial l}\frac{dr}{2} + q_r - q_{br}\right)}{h_b} \tag{24}$$

where ε is the bank migration rate (if the bank advances, $\varepsilon > 0$; if the bank retreats, $\varepsilon < 0$; if the bank is unchanged, $\varepsilon = 0$); dr is defined as the width of the control volume nearest to the edge of the bank; h_b is the near-bank flow depth; q_l and q_r are the total sediment transport rates in the longitudinal and transverse directions, respectively; and $q_{br} = q_{br}^b + q_{br}^f$ is the transversse component of the sediment transport rate at the near-bank region as a result of bank erosion. Under the assumption of a triangular cross section of the boundary element, dr in Eq. (24) is the width of the control volume adjacent to the bank shown in Fig. 1. We can reason from Eq. (24) that the bank retreats when the net longitudinal sediment transport rate is increased or the sediment is transported away from the banks in the transverse direction or a net amount of sediment materials are carried out of a control volume near the bank. Conversely, if the net sediment transported to the control volume is positive, the bank will advance.

4.6. Mesh adjustment algorithm

Since the boundary of the computation domain is changing, the mesh has to be adjusted from time to time. Fig. 2a showed the

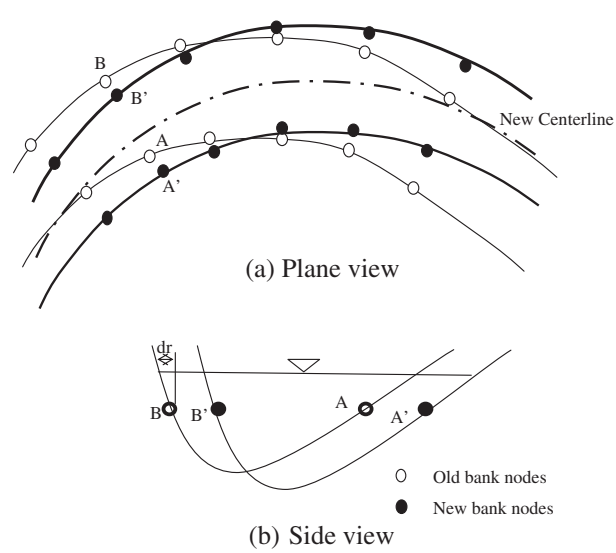

Fig. 2. Channel bankline adjustment algorithm after bank erosion.

algorithm of mesh adjustment. The dynamic mesh traces the boundary of the meandering channel and matches the computational domain to the new channel. The new mesh for the next time step is equally spaced along the banks, and it is also equally spaced in the transverse direction.

In Fig. 2b, open dots are the old boundary nodes. Solid dots are the boundary nodes after banks are moved according to the erosion distance. Solid dots are the boundary nodes after a mesh adjustment. In this figure, node *A* retreats, and node *B* advances. The old cross section *AB* is moved to *A'B'* after bank erosion. Assuming channel width remains unchanged during meandering process, bank retreat at one side of channel should be equal to the advance at the other side of channel. In the present channel meandering simulations, the bank erosion rate is the average of the absolute values of these rates at both banks of the channel because a constant channel width is assumed.

The new centerline is obtained by connecting the centers of each new cross section. The new centerline may be a little longer or shorter than the previous one due to the deformation of meandering loops. Since no additional nodes are added or deleted during computation, the position of each cross section should be relocated in order to obtain a mesh for a better computational accuracy and efficiency. The new centerline is equally divided, and the center of each cross section is re-determined. In case of a high erosion rate,

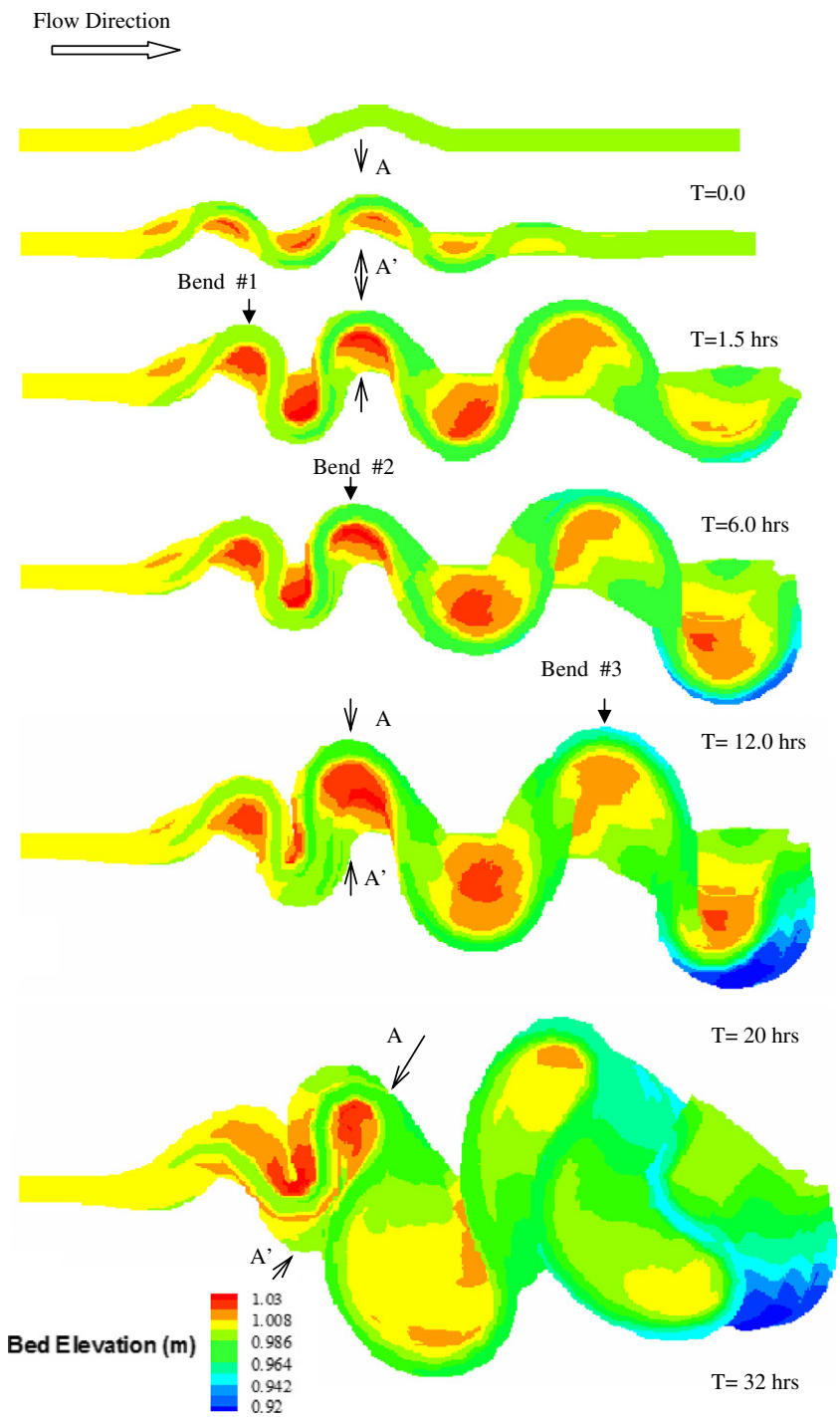

Fig. 3. Numerical simulation of the topographic evolution of a meandering channel.

the time step of bank erosion has to be reduced. The adjusted cross section $A'B'$ must be normal to the new centerline, and has a width of the initial channel width AB. Then, at each cross section, computational nodes along the transverse direction are uniformly distributed. The adjusted mesh has the same computational domain as the previous one, even though the positions of cross sections and computational nodes have been relocated in the physical domain. Each new cross section of the adjusted mesh is normal to the new centerline, and computational nodes are uniformly distributed along the transverse direction.

After the mesh adjustment, the flow field needs to be recalculated for a certain time to achieve the steady state for the new channel. This entire process is repeated for each new morphological time-step until the simulation is completed at the final time step specified.

5. Meandering channel deformation results

The evolution of a sine-generated meandering channel was simulated to test the capabilities of the developed model. The experiment was conducted in a physical model by da Silva (1995) in a sine-generated channel with an initial angle of 30°. Flow discharge is *2.10 l/s*, width of the channel is *0.4 m*, and total length of the simulated channel is *7.29 m*. The bed and bank are assumed to be erodible and are composed of the same coarse sand $d_{50} = 0.45$ mm, and the channel width is constant. The new simulated channel boundary was plotted over the older boundaries in Fig. 3 to illustrate the complicated motions of meandering loops. The evolution of the bed topography resulting from development of the meandering channel is plotted in Fig. 3, where the alternate bar and pool form is shown clearly in the channel. From Fig. 3, it is also obvious that downstream and upstream translation, lateral extension, upstream and downstream rotation, and enlargement of the meandering channel, as well as the combination of these movements, are captured in the current model. The bed elevations at the center of the channel and near the left and right banks at different times are shown in Fig. 4. At the beginning, the height of sand bars increases as the meandering channel evolves. As time progresses, the sand bar gradually migrates downstream with the increasing amplitude and wavelength of the meandering channel. The changes of a typical cross section, Section A–A in Bend #2, was shown in Fig. 5 in which the main channel shifts to the left bank as the sand bars grow at the right bank.

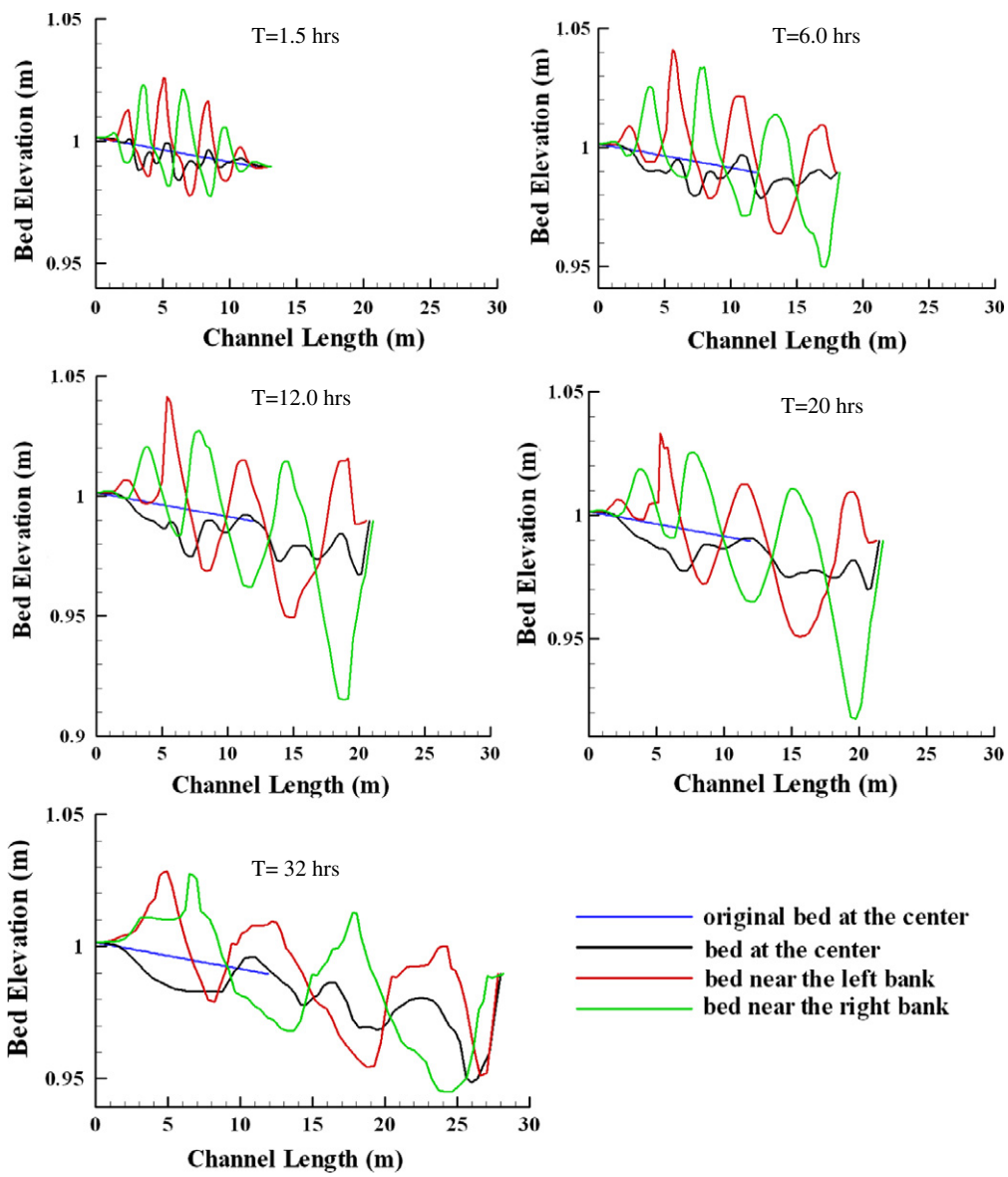

Fig. 4. Longitudinal bed-elevation changes along the channel length.

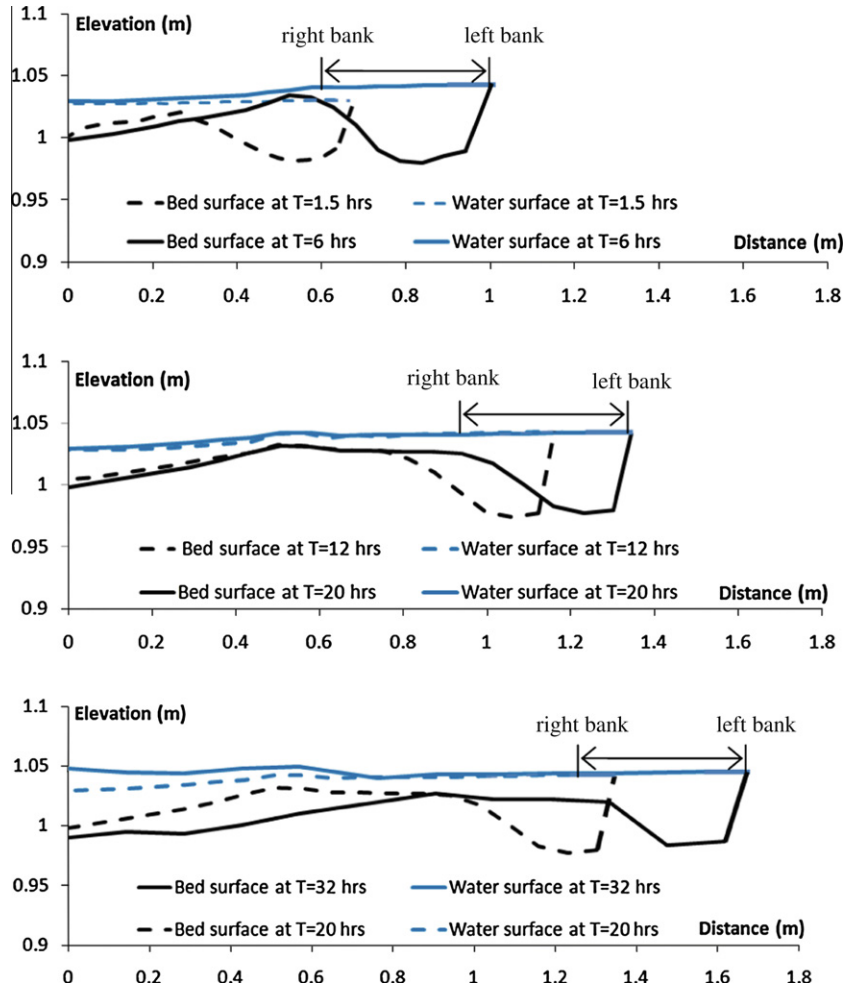

Fig. 5. Cross sectional changes as sand bars grow in the convex banks.

Neither laboratory experiments nor field measurements are able to record through real-time measurements the detailed history of meandering channel evolution. By contrast, a numerical model can record the planform evolution changes of meandering channels, as well as the flow topography and momentum, at each time step. Therefore, the simulated entire evolutionary process was divided into five phases according to the characteristic changes in meandering planform geometry.

1. At the early stage, a near-straight channel migrates rapidly in the downstream direction.
2. As sinuosity increases, downstream translation diminishes and meandering loops expand laterally in the second stage.
3. When sinuosity is sufficiently large, the rate of downstream migration reduces and the planform geometry remains essentially unchanged for some time.
4. Meandering loops migrate in the upstream direction and continue to expand laterally.
5. As channel sinuosity continues increasing, the meandering loops begin to rotate until reaching a sinuosity about 3.7. Consequently, a neck cutoff will be formed.

Similar meandering planforms can be found in natural freely meandering rivers. Fig. 6 showed five reaches of a free meandering river in Tanana Valley State Forest near Nenana City at (64.731952, −149.974365) in Alaska from Google Earth. Five reaches closely match five stages of meandering evolutions in Fig. 3, which indicated different reaches of this river are at various stages of meandering evolution. At stages 4 and 5, bifurcation occurred that will further complicate the meandering evolution process. The current model version cannot simulate the process of a neck cutoff. Correlations between the rate of bank erosion with flow momentum and bed elevations at different stages of meandering evolution are described in the following sections. In the following sub-sections, each phase of the channel development process is illustrated with changes in bed elevation and with the corresponding distribution of momentum over the reach.

5.1. Phase 1: downstream migration

This phase is characterized by downstream translation and slight rotation of meandering loops. Fig. 7a and b is the bed topography and the momentum distribution of the initial sine-generated meandering channel, respectively. Fig. 8a shows that the meanders migrate downstream when channel sinuosity is low (less than 1.4). The head of the first meandering (bend #1) loop slightly rotates downstream until sinuosity reaches 1.4. As the meandering loop migrates downstream, large sediment deposits or point bars (marked in red) shown in Fig. 8a emerge on the convex bank near the apex. They expand almost symmetrically to the apex with a slight rotation in the downstream direction. Fig. 8b shows the distribution of flow momentum, or unit discharge defined as the product of velocity and depth, in shaded colors. This figure shows

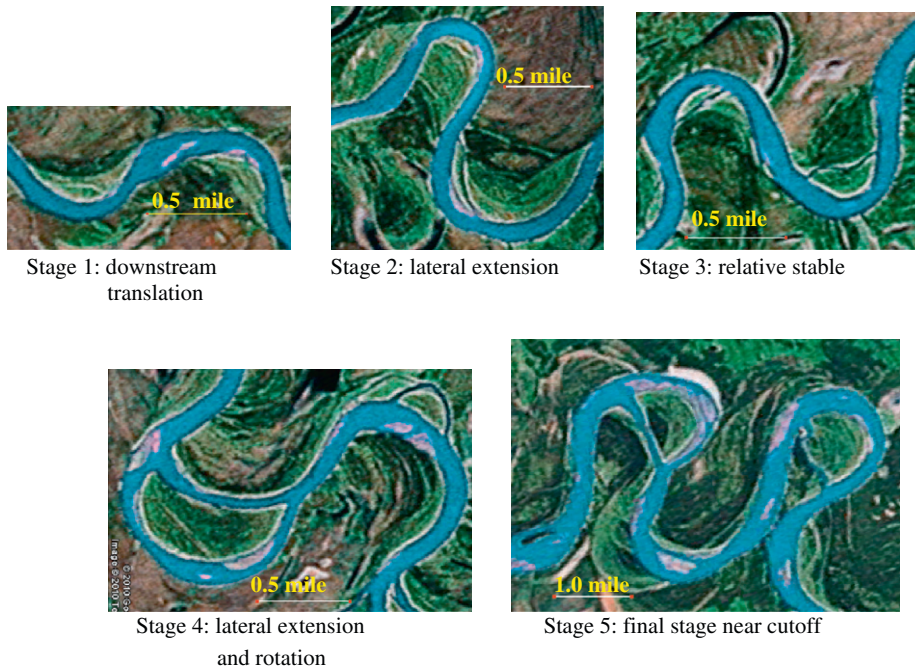

Fig. 6. One free meandering river in Tanana Valley State forest near Nenana City, Alaska.

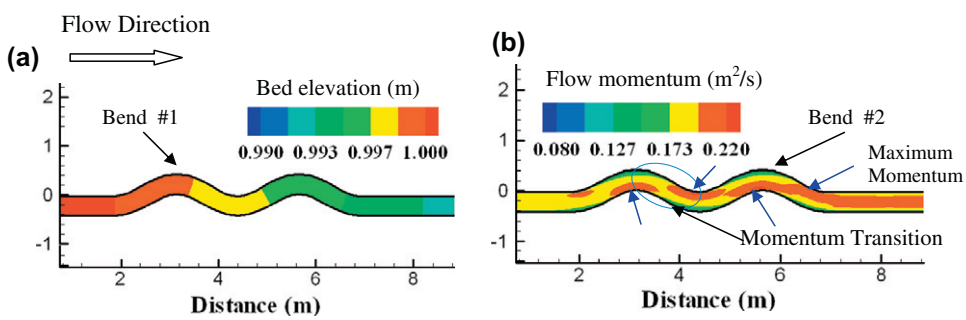

Fig. 7. Initial sine-generated meandering channel (black $T = 0$ h).

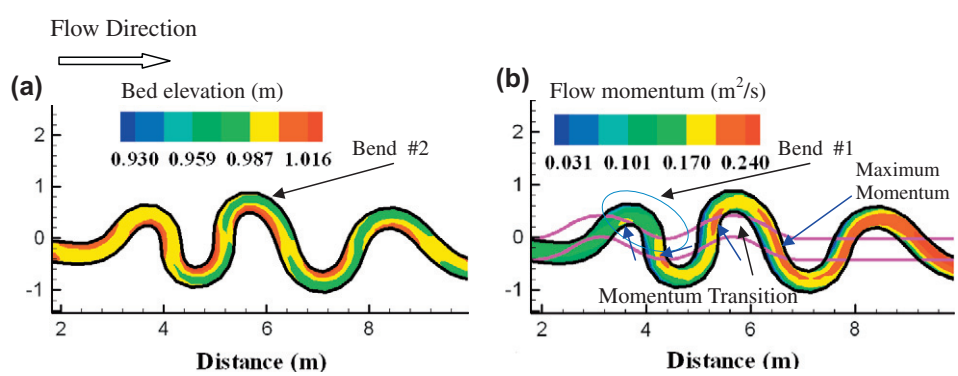

Fig. 8. First phase of downstream meandering migration (black, $T = 1.5$ h, purple $T = 0$ h). (For interpretation of the references to color in this figure legend, the reader is referred to the web version of this article.).

that the maximum momentum zone resides near the convex bank in the region upstream of the apex pointed by the blue arrow. Sand bars form where flow momentum is reducing in the downstream region of the apex. The location where the maximum momentum shifts from the convex bank (or the inner bank) to the concave bank (or the outer bank), hereafter is called the momentum transition zone, occurs slightly downstream from the apex as shown in the first bend (marked in a blue ellipse).

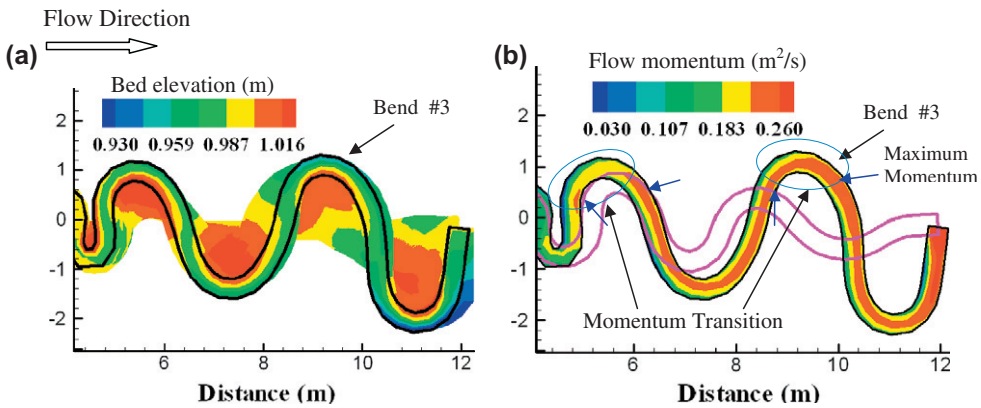

Fig. 9. Second stage of lateral expansion (black $T = 6.0$ h, purple $T = 1.5$ h). (For interpretation of the references to color in this figure legend, the reader is referred to the web version of this article.).

5.2. Phase 2: lateral extension

Fig. 9a shows the evolution of bed topography especially the growth of point bars during the processes of lateral expansion. When channel sinuosity is larger than 1.4, downstream migration reduces, while lateral extension increases appreciably at both the second and the third bend. When meandering loops extend laterally, the head of the loop slightly rotates in the upstream direction at the second bend and in the downstream direction at the third bend. As a consequence, sand bars expand laterally while tilting to the downstream or upstream directions that correspond with the directions of head rotations. Changes in distribution of flow momentum shown in Fig. 9b explain why the lateral expansion replaces downstream translation during this second phase. Sand bars form where flow decelerates and flow momentum begins to decrease. On the concave bank, the maximum momentum zone (pointed by a blue arrow) resides close to the inflection point at the second bend, while it is located upstream of the inflection point at the third bend. Therefore, in the second bend, flow is accelerating at the concave bank until reaching the maximum momentum at the inflection point. This flow acceleration will cause bank erosion. This acceleration zone also exists at the concave bank in the third bend, but has a shorter length than that in the second bend. This distribution results in a longer reach subject to bank erosion due to flow acceleration on the concave bank in the second bend that perhaps drives the head rotates toward the upstream. Consequently, the second bend rotates towards upstream, but the third bend towards the downstream.

On the other hand, at the second bend, the meandering loop rotates in the upstream direction when the momentum transition zone is located at the immediate upstream region of the apex. At the third bend, the meandering loop rotates in the downstream direction as it extends laterally where the momentum transition zone is located at the downstream of the apex. Therefore, the location of the flow momentum transition determines whether the head of a meandering loop is rotating downstream or upstream as it migrates downstream and extends laterally. Not only the geometry of the meandering planform but also the topographic features (e.g., point bars) affect the redistributions of flow momentum in meandering channels. Without the formation of point bars, the maximum flow momentum always resides close to the inner banks (Fig. 7b), so that meandering channels will not evolve into high-sinuous meandering channels (Chen and Duan, 2006). The point bar formation redistributes flow momentum and causes the momentum transition zone shift to near the apex. As a result, the migration of meandering channels is dominated by the formation of point bars, as well as by the evolution of meandering planforms. The sinuosity of a meandering loop is about 2.0 in this phase.

5.3. Phase 3: quasi-equilibrium

A quasi-equilibrium meander in Fig. 10a indicates that the planform geometry of the meander loop remains almost unchanged when the meandering loop has a sinuosity of 2.0. During this phase, the rate of lateral bank erosion is negligible, and therefore

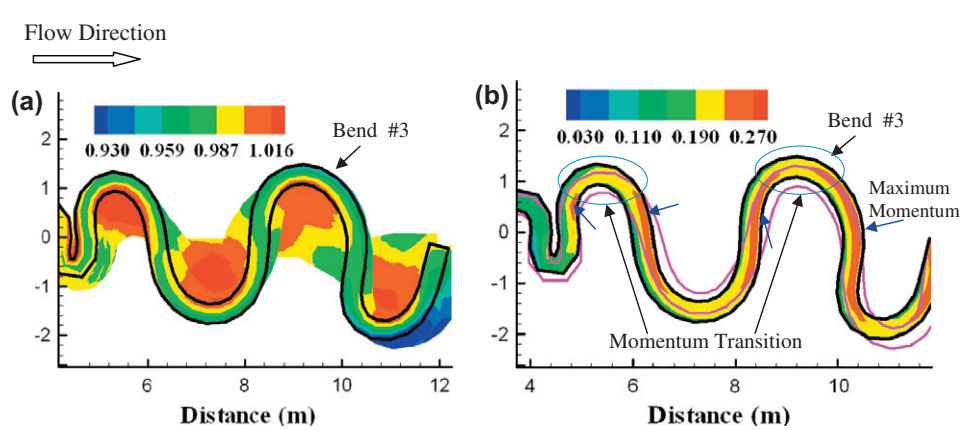

Fig. 10. Third stage of meandering migration of quasi-equilibrium (black $T = 20$ h, purple $T = 12$ h). (For interpretation of the references to color in this figure legend, the reader is referred to the web version of this article.).

the planform of the meandering loop does not change for about 8 h. Fig. 10a shows a nearly symmetrical meandering loop, and the transition reach in the upstream and downstream regions of the bend is perpendicular to the flow centerline at the apex. Additionally, the point bars continue to grow at a slow rate, and the growth of sand bars is almost symmetrical with respect to the apex. Fig. 10b shows that the flow momentum is lower and more uniformly distributed than in the first two phases. The maximum flow momentum is located near the convex bank close to the crossing and then move towards the apex of the meander bend as meandering evolves (Fig. 11b). Because of the symmetrical meandering planform and size and geometric location of sand bars, the migration rate of this meandering planform is almost zero although point bars continue to grow and the distribution of flow momentum continues to change slowly.

5.4. Phase 4: upstream migration

As point bars grow larger (Fig. 11a), the maximum flow momentum zone in the upstream half of the bend shifts toward the apex, while the maximum flow momentum zone in the downstream half of the bend moves past the crossing (Fig. 11b). Since flow momentum in the downstream half of the bend is larger than in the upstream half, the entire meandering loop begins to migrate in the upstream direction. The purple line in Fig. 11b denotes the channel boundaries at $T = 20$ h, and the black line denotes the channel boundaries at $T = 26$ h. The meandering loop also expands laterally as it migrates in the upstream direction. Since the maximum momentum zones reside near the crossing and the momentum transition zone is located almost at the apex, the meandering loop remains symmetrical as it migrates in the upstream direction. Although no upstream or downstream rotation is observed, the neck of the meandering loop becomes narrow, which indicates that the rate of migration at the downstream crossing is greater than at the upstream crossing.

5.5. Phase 5: meandering channel rotation

As soon as the maximum momentum zone shifts toward the apex, the momentum transition zone moves to the downstream region of the apex (Fig. 12b). Therefore, the head of the meandering loop begins to rotate in the downstream direction, and its migration rate in the upstream direction begins to reduce. Fig. 12a shows that asymmetrical point bars are starting to develop with a lobate feature pointed in the downstream direction. The purple lines in Fig. 12b are the boundaries of the meandering channels at

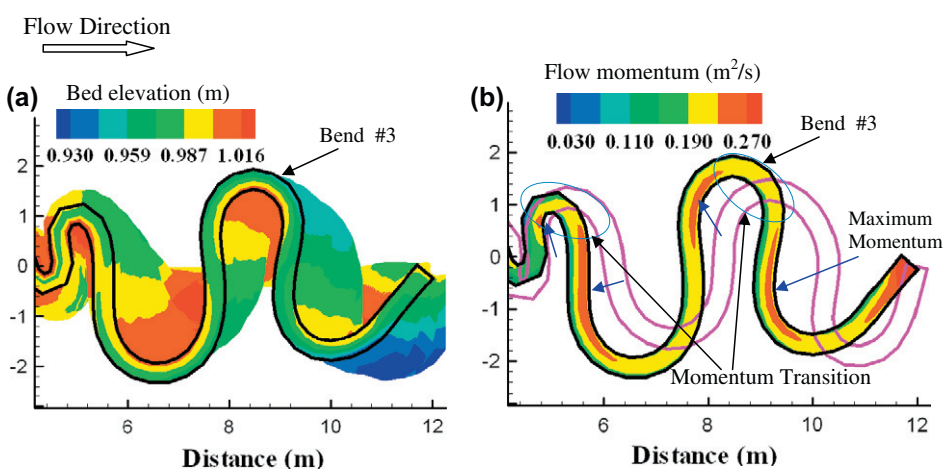

Fig. 11. Fourth stage of upstream meandering migration (black $T = 26$ h, purple $T = 20$ h). (For interpretation of the references to color in this figure legend, the reader is referred to the web version of this article.)

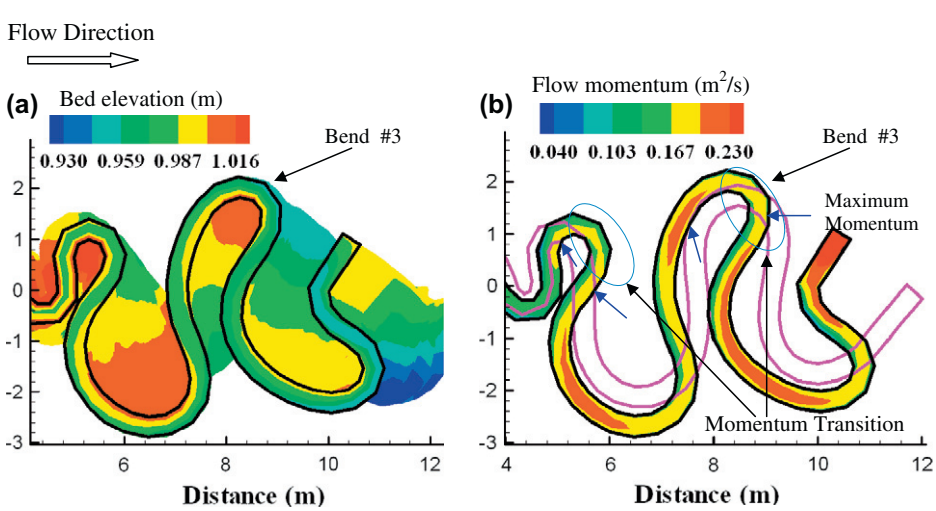

Fig. 12. Fifth stage of rotation and meandering migration (black $T = 32$ h, black $T = 26$ h).

T = 26 h, while the black lines are the boundaries at T = 32 h. Notice that these features take a long time to develop compared to Phases 1 and 2. This is because the sinuosity is very high and the momentum is much lower than in Phases 1 and 2. Since the crossing reach in the downstream half of the bend migrates upstream faster than that in the upstream reach and because the head of meandering loop rotates in the upstream direction, a goose-neck shaped meandering loop is formed. This goose-neck shaped meandering loop is a very common planform in natural meandering streams where some bends have a head in the upstream direction and some have a head in the downstream direction. It has been observed that 40% of Mississippi River bends have their heads toward the downstream direction and 60% toward the upstream direction (Larsen, 1995). Whether the head of the meandering loop is upstream or downstream depends on the location of flow momentum transition zones. This simulation through the present study indicates that if the momentum transition zone is located exactly at the apex, the meandering loop will expand only laterally. However, if the momentum transition zone is located immediately upstream from the apex, the meandering loop will migrate and rotate in the upstream direction. Otherwise, the meandering loop will migrate and rotate in the downstream direction.

In summary, the evolution of a meandering channel begins with downstream translation and is followed with lateral expansion, and upstream/downstream rotation before it reaches a quasi-stable state where sinuosity is approximately 2.0. The quasi-stable meandering planform has a minimum bank erosion rate, and the meandering planform is almost symmetrical with respect to the apex. When sinuosity in a meandering channel slowly continues to increases, the quasi-steady meandering planform migrates in the upstream direction and continuously expands laterally. The upstream migration rate eventually decreases and the head of the meandering loop rotates in the downstream direction. A goose-neck shaped meandering loop is formed at end of the simulation.

This evolution process of the meandering planform geometry is closely linked to the distribution of flow momentum, especially at the location where the maximum flow momentum zone shifts from one bank to the other. The simulated results indicate that the location where the maximum momentum zone shifts from the convex to the concave bank in a meandering channel varies with strength in the secondary current, which is induced by the curvature of meanders and the transverse bed slope due to the development and expansion of sand bars. Laboratory experiments (Friedkin, 1945; Schumm et al., 1987) have also shown that a meandering channel can evolve from a mildly curved channel to a highly sinuous channel. As soon as a sinuous channel develops, the transverse slope appears with the accompanying formation of sand bars. The core of the maximum momentum zone moves to the center and then to the concave bank due to the increased curvature and topographically induced secondary flow. This influence of topographically induced secondary flow is believed to be at least as important as secondary flow induced by curvature (Hooke, 1975; Dietrich and Smith, 1983; Dietrich and Whiting, 1989; Nelson and Smith, 1989).

Natural meandering channels have different planform configurations and various types of sand bars (e.g., point bars, multiple bars). The location of the maximum momentum zones and the transitions of momentum from convex or concave banks may occur anywhere within a meandering bend. This momentum shift determines if the evolution of a meandering channel is downstream/upstream translation, lateral expansion, upstream/downstream rotation, or any combination of these motions. The presence of developed sand bars near the convex bank in highly sinuous channels causes a large transverse slope, which facilitates the shift of the maximum shear stress zone to the concave bank.

6. Discussion

The computational modeling results of meandering migration processes indicated that it is feasible to use a depth-averaged, two-dimensional model to simulate the hydrodynamic flow field, sediment transport, bank erosion, and consequently meandering evolution processes. Although the hydrodynamic flow field in meandering channels is highly three-dimensional, the dispersion terms in momentum equations arising from the secondary flow can be included to compensate this effect (Duan, 2004). Natural meandering rivers often have variable widths, and the unsteady flow during storm events is usually the driving mechanism of meandering evolution. This requires a robust numerical scheme that can capture rapidly varied floodwaves. The upwinding shape functions for the efficient element method (Duan et al., 2001; Duan, 2004) adopted in this model is not capable of simulating unsteady flow, which limits the applicability of the current version to steady or quasi-unsteady flows. Besides since the morphologic processes of meandering rivers involves continuous changes of flow paths due to bank erosion and point bar formations, the numerical scheme must incorporate an algorithm for handling alterations of dry and wet nodes. Otherwise, a constant width assumption is needed to confine the simulation domain to the wet nodes.

Additionally, the cutoff of meandering bends is an important feature in meandering evolution, which can be simulated by using an adjustable mesh. Available finite element and finite volume methods have limitations when applying to rapidly changing unsteady flow under complex geometries (Toro and Chakraborty, 1994; Toro and Garcia-Navarro, 2007). Future research on robust numerical schemes, such as the high-order WENO scheme, is needed to extend the models' capability to real life natural rivers.

7. Conclusions

The present two-dimensional numerical model incorporates physically-based bank erosion model components into a depth-averaged flow model with bed load and suspended sediment transport to simulate the processes of meandering evolution. A very important aspect of this model is that bank erosion does not guarantee the retreat of a bank line if eroded bank material remains at the toe of the bank. Whether or not a bank retreats or advances depends on the balance of sediment load near the banks where sediment may be transported both in the downstream direction and also laterally due to secondary flows.

The primary conclusions of this study are: (1) this 2D numerical model clearly demonstrates the evolution of meandering channels from low to high sinuosity; (2) the growth of point bars affects the distribution of shear stress, secondary currents and flow momentum; and (3) the model properly simulates the various modes of deformation of meandering channels, such as downstream and upstream migration, lateral extension and rotation of meander bends. The essential processes leading to formation of meandering channels are well replicated with this model. The modeling results contributed to better understanding of the processes associated with lateral channel migration, as well as aids in explaining the formation of river meanders.

Acknowledgements

The authors are grateful for research funding provided by NSF SGER Award EAR-820412 and the Army Research Office under the proposal number **52326EV**. This project is also in collaboration with the State Key Laboratory of Hydroscience and Engineering at Tsinghua Univ.

References

Bridge, J.S., Bennett, S.J., 1992. A model for the entrainment and transport of sediment grains of mixed sizes, shapes, and densities. Water Resour. Res. 28 (2), 337–363.

Baek, K.O., Seo, I.W., Jeong, S.J., 2006. Evaluation of dispersion coefficients in meandering channels from transient tracer tests. J. Hydraul. Eng., ASCE 132 (10), 1021–1032.

Chen, D., Duan, J.G., 2006. Simulating meandering channel evolution with an analytical model. J. Hydraul. Res. 44 (5), 624–630.

Chen, D., Duan, J., 2008. Case study: two-dimensional model simulation of channel migration processes in the West Jordan River, Utah. J. Hydraul. Eng. 134 (3), 315–327.

Chien, N., Wan, Z.H., 1991. Dynamics of Sediment Transport. Academic Press of China, Beijing (in Chinese).

Camporeale, C., Perona, P., Porporato, A., Ridolfi, L., 2005. On the long-term behavior of meandering rivers. Water Resour. Res. 41, W12403. doi:10.1029/2005WR004109.

Darby, S., Delbono, I., 2002. A model of equilibrium bed topography for mean bends with erodible banks. Earth Surf. Proc. Land. 27 (10), 1057–1085.

Darby, S.E., Alabyan, A.M., Van De Wiel, M.J., 2002. Numerical simulation of bank erosion and channel migration in meandering rivers. Water Resour. Res. 38 (9), 2–1-12.

da Silva, A.M.F., El-Tahawy, T., Tape, W.D., 2006. Variation of flow pattern with sinuosity in sine-generated meandering streams. J. Hydraul. Eng. 132 (10), 1003–1014.

da Silva, A., 1995. Turbulence Flow in Sine-generated Meandering Channel. Ph.D. Thesis, Queen's University, Kingston, Ontario, Canada.

Dietrich, W.E., Smith, J.D., 1983. Influence of the point bar on flow through curved channels. Water Resour. Res. 19 (5), 1173–1192.

Dietrich, W.E., Whiting, P., 1989. Boundary shear stress and sediment transport in river meanders of sand and gravel. In: Ikeda, S., Parker, G. (Eds.), River Meandering. AGU, pp. 1–50.

Duan, J.G., Wang, S.Y., Jia, Y., 2001. The application of the enhanced CCHE2D model to study the alluvial channel migration processes. J. Hydraul. Res. 39 (5), 469–480.

Duan, J.G., 2004. Simulation of flow and mass dispersion in meandering channels. J. Hydraul. Eng., ASCE 130 (10), 964–976.

Duan, J.G., 2005. Analytical approach to calculate the rate of bank erosion. J. Hydraul. Eng., ASCE 131 (11), 980–990.

Duan, J.G., Julien, P.Y., 2005. Numerical simulation of the inception of meandering channel. Earth Surf. Proc. Land. 30, 1093–1110.

Duan, J.G., Nanda, S.K., 2006. Two-dimensional depth-averaged model simulation of suspended sediment concentration distribution in a groyne field. J. Hydrol.. doi:10.1016/j.jhydrol.2005.11.055.

Engelund, F., 1974. Flow and bed topography in channel bend. J. Hydraulic Div., ASCE 100 (11), 1631–1648.

Friedkin, J., 1945. A Laboratory Study of the Meandering of Alluvial Rivers. Technical Reports, US Waterways Experiment Station, Vicksburg, Mississippi.

Hooke, R., 1975. Distribution of sediment transport and shear stress in a meander bend. J. Geol. 83 (5), 543–566.

Ikeda, S., Parker, G., Sawai, K., 1981. Bend theory of river meanders, vol. 1. Linear development. J. Fluid Mech. 112 (11), 363–377.

Julien, P.Y., 2002. River Mechanics. Cambridge University Press, 434p.

Julien, P.Y., Anthony, D.J., 2002. Bed load motion and grain sorting in a meandering stream. J. Hydraul. Res., IAHR 40 (2), 125–133.

Johannesson, H., Parker, G., 1989. Velocity redistribution in meandering rivers. J. Hydraul. Eng. 115 (8), 1019–1039.

Kironoto, B.A., Graf, W.H., 1994. Turbulent characteristics in roughness uniform open-channel flow. Proc. Inst. Civ. Eng., Waters, Maritime Eng., 98.

Larsen, E.W., 1995. Mechanics and Modeling of River Meander Migration. Dissertation, Univ. of California, Berkeley.

Marion, A., Zaramella, M., 2006. Effects of velocity gradients and secondary flow on the dispersion of solutes in a meandering channel. J. Hydraul. Eng., ASCE 132 (12), 1295–1302.

Mosselman, E., 1998. Morphological modeling of rivers with erodible banks. Hydrol. Process. 12, 1357–1370.

Nagata, N., Hosoda, T., Muramoto, Y., 2000. Numerical analysis of river channel processes with bank erosion. J. Hydraul. Eng., ASCE 126 (4), 243–252.

Nelson, J.M., Smith, J.D., 1989. Flow in meandering channels with natural topography. In: Ikeda, S., Parker, G. (Eds.), River Meandering. AGU, Water Resources Monograph, p. 12.

Nicholas, A.P., Smith, G.S., 1999. Numerical simulation of three-dimensional flow hydraulics in a braided channel. Hydrol. Process. 13, 913–929.

Odgaard, A., 1989. River meander model, I: development. J. Hydraul. Eng., ASCE 115 (11), 1433–1450.

Olsen, N.B., 2003. Three-dimensional CFD modeling of self-forming meandering channel. J. Hydraul. Eng., ASCE 129 (5), 366–372.

Osman, M.A., Thorne, C.R., 1988. Riverbank stability analysis. I: theory. J. Hydraul. Eng., ASCE 114 (2), 134–150.

Pizzuto, J.E., 1990. Numerical simulation of gravel river widening. Water Resour. Res. 26, 1971–1980.

Schumm, S.A., Mosley, M.P., Weaver, W.E., 1987. Experimental Fluvial Geomorphology. John Wiley & Sons.

Seo, I.W., Lee, M.E., Bae, K.O., 2008. 2D Modeling of heterogeneous dispersion in meandering channels. J. Hydraul. Eng., ASCE 134 (2), 196–204.

Sun, T., Meakin, P., Jossang, T., Schwarz, K., 1996. A simulation model for meandering rivers. Water Resour. Res. 32 (9), 2937–2954.

van Rijn, L.C., 1989. Sediment Transport by Currents and Waves. Report H461, Technical Report, Delft Hydraulics.

Toro, E.F., Chakraborty, A., 1994. The development of a Riemann solver for the steady supersonic Euler equations. Aeronaut. J. 98 (979), 325–339.

Toro, E.F., Garcia-Navarro, P., 2007. Godunov-type methods for free-surface shallow flows: a review. J. Hydraul. Res. 45 (6), 736–751.

Wilson, C.A.M.E., Boxall, J.B., Guymer, I., Olsen, N.R.B., 2003. Validation of a three-dimensional numerical code in the simulation of pseudo-natural meandering flows. J. Hydraul. Eng., ASCE 129 (10), 758–768.

Zarrati, A.R., Tamai, N., Jin, Y.C., 2005. Mathematical modeling of meandering channels with a generalized depth averaged model. J. Hydraul. Eng., ASCE 131 (6), 467–475.

Zolezzi, G., Seminara, G., 2001. Downstream and upstream influence in river meandering. Part 1. General theory and application to overdeepening. J. Fluid Mech. 438, 183–211.